

Vector Field Visualization of Advective-Diffusive Flows

H. Hochstetter, M. Wurm and A. Kolb

Computer Graphics and Multimedia Systems Group, University of Siegen, Germany

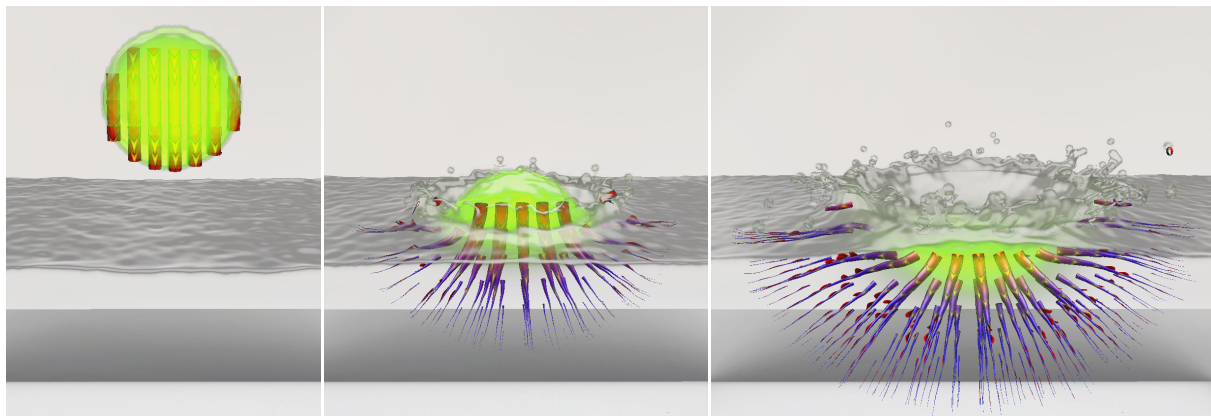


Figure 1: A drop of green dye is dripped into water. Before impact, only advection plays a role (left). Directly after impact, the drop's velocity, i.e. advection, still dominates concentration transport (middle), but diffusion increasingly becomes the main mode of transport (right). Red and blue indicate advection and diffusion dominated flow, respectively.

Abstract

We propose a framework for unified visualization of advective and diffusive concentration fluxes, which play a key role in many phenomena like, e.g. Marangoni convection and microscopic mixing. The main idea is the decomposition of fluxes into their concentration and velocity parts. Using this flux decomposition, we are able to convey advective-diffusive concentration transport using integral lines. In order to visualize superimposed flux effects, we introduce a new graphical metaphor, the stream feather, which adds extensions to stream tubes pointing in the directions of deviating fluxes. The resulting unified visualization of macroscopic advection and microscopic diffusion allows for deeper insight into complex flow scenarios that cannot be achieved with current volume and surface rendering techniques alone.

Our approach for flux decomposition and visualization of advective-diffusive flows can be applied to any kind of (simulation) data if velocity and concentration data are available. We demonstrate that our techniques can easily be integrated into Smoothed Particle Hydrodynamics (SPH) based simulations.

Categories and Subject Descriptors (according to ACM CCS): I.6.6 [Simulation and Modeling]: Simulation Output Analysis—J.2 [Physical Sciences and Engineering]: Physics—

1. Introduction

Understanding the behavior of concentration transport in fluid flows is a challenging task. There exists a wide array of scientific visualizations to aid in gaining insight

into experimental and simulated flow data. The most important approaches are volume rendering of concentration fields [EHK*06], vector field visualization of advection by means of line integral convolution [CL93], by tracing integral lines, and also by flow based surfaces [MLP*10].

However, so far mainly advective flows have been investigated while the complex flow of concentrations inside fluids, which additionally depends on diffusive flux, has not been considered in the context of integral line visualizations but only in direct volume rendering [KSW*12] and visualization of topological features [SKE14] of dye-advection. Concentrations in the fluid have an impact on important physical quantities like surface tension, which, e.g., leads to the effect of Marangoni convection. Many real-world applications depend on the complex interplay between advection and diffusion although their respective contributions to an observed behavior are not always clear. Our visualization of advective-diffusive transport aims at filling this gap, enabling researchers to identify and understand the driving forces in complex transport scenarios encountered in, e.g. microscopic mixing [KWFY99], and dynamic wetting [FAB*11].

We propose a visualization framework for advection and diffusion based on tracing integral lines. The main idea is to provide insight into the intrinsic structure of the concentration transport consisting of both, the diffusive and the advective component. In order to combine both components to a unified flux of concentration, we propose concepts for decomposing the diffusive flux into a velocity and a concentration part. The visualization then uses integral lines that provide means for disclosing the intrinsic diffusive and advective components of the combined flux. The main contributions of our approach are:

- A generic framework to describe arbitrary types of fluxes that is based on the decomposition of fluxes into velocity and concentration.
- Our decomposition of diffusive flux based on the concept of mean and maximum diffusion velocity allows for integral line visualization of diffusive transport.
- Vector field visualization of combined advection-diffusion processes introducing *stream feathers* to visualize diffusion and advection simultaneously.

We apply our visualization approach to *Smoothed Particle Hydrodynamics (SPH)* simulations of incompressible fluids. In this context we contribute

- a stable reconstruction of continuous advective and diffusive flux fields in SPH as required for our visualization.

Note that the proposed decomposition of fluxes and thus our visualization approach for advective-diffusive flows can be applied to any kind of (simulation) data as long as velocity and concentration data are available.

This paper is structured as follows: Sec. 2 discusses the relevant theory and related work. Sec. 3 gives a general overview of our framework. We show how to decompose fluxes to make them available for integral line visualization in Sec. 4. The resulting fields can be rendered using our novel stream feather metaphor introduced in Sec. 5. Details of our SPH-based simulation and visualization framework

are described in Sec. 6. Results are presented and discussed in Sec. 7. Sec. 8 concludes the paper.

2. Foundations and Prior Work

In this section we give a brief overview of advective and diffusive flux (Sec. 2.1) and on respective visualization techniques (Sec. 2.2). As we apply our generic advective-diffusive flux visualization to SPH-based flow simulations, we furthermore discuss visualization techniques applied to SPH-fluids (Sec. 2.3).

2.1. Advective and Diffusive Flux

Advective flux carries concentration $c(\mathbf{x})$ with the velocity field $\vec{v}(\mathbf{x})$ through unit area per unit time at position \mathbf{x} as

$$\vec{j}_a(\mathbf{x}) = c(\mathbf{x})\vec{v}(\mathbf{x}). \quad (1)$$

In the presence of concentration gradients, a net transport from areas of higher concentrations to areas of lower concentrations takes place. This *diffusive flux* is calculated according to Fick's law as

$$\vec{j}_d(\mathbf{x}) = -D\nabla c(\mathbf{x}), \quad (2)$$

where D is the molecular diffusivity. The *total flux* of concentration through unit surface per unit time at position \mathbf{x}

$$\vec{j}_t(\mathbf{x}) = \vec{j}_d(\mathbf{x}) + \vec{j}_a(\mathbf{x}) \quad (3)$$

is the sum of advective and diffusive fluxes and follows the direction of maximum transport [BSL07].

2.2. Visualization of Advective-Diffusive Flow

Scalar fields like concentrations are usually visualized using direct or texture based volume rendering techniques as comprehensively described by Engel et al. [EHK*06].

In flow visualization, line integral convolution (LIC) has been used [CL93] in which noise textures are convolved with vector fields. LIC has been extended by a model of non-linear diffusion which, however, is not part of the simulation data but is, for example, applied to segment the resulting flow fields [BPR01, DPR00]. Flows have also been visualized by geometric means like tubes and ribbons that follow integral lines. For further details we refer to the survey by McLoughlin et al. [MLP*10]. Illustrative techniques enhance renderings by adding directional information, by reducing cluttering or by improving depth perception [BCP*12].

Advective-diffusive flows have been visualized using surface renderings of clouds of concentration spreading. However, the diffusive part does not follow a gradient but just extends streamlines that follow advection to cone-shaped clouds [MS93]. Several approaches have been proposed for visualization of diffusion tensors that describe the behavior of anisotropic diffusion. Hyperstreamlines follow the

direction of the major eigenvector of the diffusion tensor field [DH93] and have been extended to Tensorlines to increase the stability in isotropic regions where all eigenvalues are nearly identical [WKL99]. Other approaches have employed tensor glyphs [KW06] and tensor volumes [KWH00] to visualize diffusion tensors. None of these approaches, however, visualized actual transport of concentrations.

Advective-diffusive flow has been visualized using direct volumetric visualizations of dye-advection [KSW*12]. Topological features of advective-diffusive flows have been examined, however, the advection-diffusion equation has only been solved in form of a secondary simulation step on top of a purely advective flow [SKE14].

Our visualization approach is based on the geometric construction of integral lines from advection-diffusion simulation data. To the best of our knowledge, neither the effects of diffusion nor the combined advective-diffusive transport have been considered in the context of integral line based visualization, so far.

2.3. Visualization of SPH Fluid Simulations

In the context of SPH-based fluid simulations, concentrations can be visualized using volume rendering [FAW10, OKK10] while surface rendering reveals the fluid's geometric shape [AIAT12]. SPH data can always be visualized by sampling field quantities on a grid and applying standard techniques. However, resampling can introduce artifacts in undersampled regions and increases computational complexity in case of unnecessary oversampling [SFBP09]. Pure advection has been visualized by directly rendering particle trajectories in combination with space-time hierarchical clustering to reduce visual clutter [FW12]. Vortex core lines have been visualized directly from SPH-data using Hermite splines to interpolate between particle positions in time [SFBP09].

As the time dependent behavior of fluids and the distinct roles of advection and diffusion to concentration transport cannot be captured by current visualization techniques, we propose an integral line based approach to simultaneously visualize advective and diffusive concentration transport. In order to achieve an interactive visualization that does not rely on any preprocessing or resampling, we directly compute the flux-related quantities within the SPH simulation. In this context, it is not sufficient to trace SPH particles to deduce concentration transport comprising diffusion and advection. As diffusion is a microscopic phenomenon modeled as concentration exchange between SPH particles, concentration transport has to be traced along arbitrary, i.e. inter-particle spacial positions.

3. Overview

Our visualization framework for advection and diffusion using integral lines requires a velocity field and a scalar

concentration field which both may be unsteady. Firstly, in Sec. 4 we discuss how to compute advective and diffusive fluxes directly from velocity and concentration data without any preprocessing. One main challenge here is the requirement to express a flux \vec{j} as decomposition of velocity \vec{v} and concentration c , i.e.

$$\vec{j} = c \cdot \vec{v} \quad (4)$$

in order to trace integral lines of fluxes. The advective flux is already given in this form. For diffusion, however, this kind of decomposition is not unique. We propose two different decompositions of diffusive flux, according to the *mean velocity of molecules* [Ein05] and to the *maximum velocity*, as for instance applied in environmental sciences in the context of the spreading of toxic waste [Sch96], which are common interpretations to diffusive processes; see Sec. 4.1.

Using the flux decomposition in Eq. (4) and the interpretations for the diffusive flux, we calculate the unified flux consisting of the advective and the diffusive component. The mean diffusive velocity, which follows the *direction of maximum transport*, yields the so-called total flux \vec{j}_t , and the maximum diffusive velocity, which follows the direction of *fastest advancing concentration front*, we get the maximum velocity flux; see Sec. 4.2.

Based on the velocity components for the advective, diffusive and unified fluxes we demonstrate the tracing of integral lines over time; see Sec. 5. Integral lines are visualized geometrically using stream tubes the thickness of which can be varied, e.g. according to the transported concentration in order to convey the actual magnitude of flux. As we want to visualize the relation of all three, potentially divergent fluxes, we extend the geometric primitive of the stream tube by introducing *stream feathers*. Stream feathers are appendages of the integral line, i.e. the stream tube in our case, indicating the directions and magnitude of deviating fluxes.

4. A Framework for Tracing Advective-Diffusive Fluxes

The core concept of our visualization approach is an extension of the concept of integral lines in order to achieve insight into multi-component, i.e. advective-diffusive fluxes. Standard integral lines are *streamlines*, *pathlines* and *streaklines*. Even though our concept directly applies to all types of integral lines, we focus on streamlines in this paper.

The position $\mathbf{x}(t)$ of samples moving along a streamline is determined by time integration. For some initial position $\mathbf{x}(t_0)$ at time t_0 a streamline can be traced as

$$\mathbf{x}(t) = \mathbf{x}(t_0) + \int_{t_0}^t \vec{v}(\mathbf{x}(t_0), \tau) d\tau, \quad (5)$$

where $\vec{v}(\mathbf{x}, t)$ is the flow field's velocity. As advective flux \vec{j}_a already is in a separated form, i.e. $\vec{j}_a = c \cdot \vec{v}_a$, it can directly be used to trace integral lines over time [JH04].

The same does not hold for diffusive flux as there is no unique definition of a velocity which could be used to determine streamlines. In order to make diffusive flux \vec{j}_d and total flux \vec{j}_t available for integral line visualizations, they have to be expressed in a decomposed form just as the advective flux, i.e. as $\vec{j}_d = c_d \cdot \vec{v}_d$ and $\vec{j}_t = c_t \cdot \vec{v}_t$.

Note that although the flux is unchanged by the way it is decomposed, the resulting integral lines may depend on the decomposition, i.e. on the velocity part.

In the following, we will discuss the decomposition of the diffusive flux (Sec. 4.1). Afterwards we describe how to derive a similar form of the unified flux in Sec. 4.2.

4.1. Decomposition of Diffusive Flux

One major challenge with diffusion is its random nature. As diffusion arises from Brownian molecular motion, there is no unique way to define a diffusion velocity for the decomposition of diffusive flux [Cus09].

Assuming that solute molecules move randomly in solution in steps of Δx length, their mean free path until a collision with neighboring molecules occurs, at a *molecular velocity* v_d^{mol} , then the position of molecules after some time t can only be described in terms of density distributions. Based on this consideration, the *molecular diffusivity* is defined as (see also Eq. 2)

$$D = v_d^{\text{mol}} \Delta x. \quad (6)$$

Even though movement occurs as a random process, transport from areas of higher concentrations to areas of lower concentrations is more likely than in the opposite direction causing a net diffusive flux \vec{j}_d in the presence of concentration gradients as depicted in Fig. 2.

There are two major interpretations of diffusion related velocity. The *mean velocity* considers the average speed of diffusing molecules, whereas the *maximum velocity* seeks to capture the advancing front of diffusion transport.

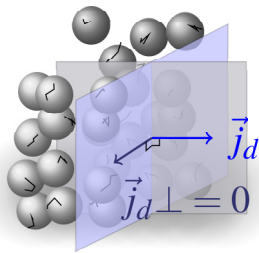


Figure 2: Diffusion follows the random movement of molecules, here depicted as the black molecule trajectories. The high concentration left of the blue plane leads to a net flux to the right. However, there is no net flux through the gray plane as the concentration on either side is the same.

Mean Velocity: According to Einstein, the mean velocity depends on the local concentration as well as the concentration gradient [Ein05]. At low Reynolds numbers, which is the case for small solute molecules in solvents like water, the mean molecular velocity of diffusion is proportional to the force due to the gradient of the chemical potential μ as

$$\vec{v}_d^{\text{mean}} = -\sigma \nabla \mu = -\sigma \frac{k_B T}{c} \nabla c = -\frac{D}{c} \nabla c = \frac{\vec{j}_d}{c}, \quad (7)$$

where σ is a temperature-dependent friction coefficient. k_B is the Boltzmann constant and T the temperature which in our case is also constant. As the force due to the chemical potential gradient acts the same on all molecules, all molecules are assumed to move at mean velocity in Einstein's model, i.e. the full concentration c is diffused resulting in $c_d^{\text{mean}} = c$. Nevertheless, in reality there will always be a fraction of molecules that move faster than the mean.

Einstein's model relates the mean diffusion velocity inversely proportional to the concentration, see Eq. 7, thus, we encounter the practical problem that for $c \rightarrow 0$ velocity diverges. Therefore, we bound the mean velocity by the maximum velocity $v_d^{\text{max}} > 0$, which we will also use for the maximum diffusion velocity.

Maximum Velocity: The maximum velocity obviously depends on the diffusivity, see Eq. 6. However, even if the molecular velocity v_d^{mol} is known, it cannot be taken as maximum diffusion velocity as the free length until molecular collision Δx needs to be taken into account, i.e. no molecule travels without collision. Practically, this length can hardly be determined.

Thus, the user can control the magnitude of diffusion velocity v_d^{max} , which is the same already used to clamp the mean velocity in case of low concentration values. Assuming a fraction of molecules moves always at this speed in the flux direction, we deduce a corresponding concentration as

$$c_d^{\text{max}} = \frac{\|\vec{j}_d\|}{v_d^{\text{max}}}, \quad \vec{v}_d^{\text{max}} = \frac{\vec{j}_d}{c_d^{\text{max}}}. \quad (8)$$

Comparing the mean and the maximum velocity interpretation for the diffusive flux, the main difference is that the mean velocity sets the concentration to the maximum value, i.e. to the total concentration, whereas the maximum velocity approach fixates the velocity. For the diffusive flux the choice of the maximal velocity v_d^{max} effects the speed a sample travels along the integral line, the line itself does not change, except for numerical integration errors. The user controlled maximal velocity does actually enhance the evaluation, as for a fixed integration time the length and thickness of the diffusion streamline can be adapted. Figs. 8(c) and 8(d) show flow fields with the diffusive flux using Einstein's mean velocity and maximal diffusive velocity, respectively. However, considering the unified maximum velocity

flux as defined in Sec. 4.2, the choice of v_d^{\max} also influences the direction of maximum velocity; see also Fig. 3.

4.2. Unified Model of Advective-Diffusive Flux

As we want to visualize advection and diffusion in a unified approach, the *unified flux* has to be decomposed in the same way as the diffusive flux. Similarly to the mean and maximum diffusion velocities we derive decompositions for the unified fluxes for both interpretations of diffusion.

Unified Flux of Mean Velocity / Total Flux: In the case of mean diffusive velocity, the whole concentration at a point in space $c_t = c_a = c_d^{\text{mean}}$ is transported at the same velocity which is just the superposition of the advection and diffusion velocities. The resulting *unified mean velocity flux* or *total flux* can thus directly be decomposed as

$$\vec{j}_t = c_t \vec{v}_t = c_t (\vec{v}_a + \vec{v}_d^{\text{mean}}) \quad (9)$$

and follows the direction of maximum transport of concentration.

Unified Flux of Maximum Velocity: In the case of a constant maximum diffusion velocity, we are not actually interested in the direction of maximum transport of concentration but rather in the direction of preferred concentration spreading. Thus we do not visualize the total flux as $\vec{j}_t = \vec{j}_a + \vec{j}_d$ but follow the direction of flux with maximum velocity

$$\vec{v}_m = \vec{v}_a + \vec{v}_d^{\max}. \quad (10)$$

To find the decomposition of constant velocity flux

$$\vec{j}_m = c_m \vec{v}_m, \quad (11)$$

we still need to determine the amount of transported concentration c_m in direction \vec{v}_m . As c_m should be physically plausible, we require $c_m \geq 0$ and compliance with the total flux in Einstein's mean velocity consideration, i.e. for $c_t = c_a = c_d^{\text{mean}} = c$ we require $c_m = c$ as well. Considering Fig. 2, it is obvious that the diffusive flux changes its magnitude depending on the considered direction of flow through a local plane. If we apply a linear model, the effective concentration flow through a unit area with normal \hat{n} with respect to the flux direction \hat{v} is proportional to $(\hat{n} \cdot \hat{v})$ [BSL07]. All of the required properties are fulfilled by defining

$$c_m = \frac{\max(0, \hat{v}_a \cdot \hat{v}_m) c_a \|\vec{v}_a\| + \max(0, \hat{v}_d \cdot \hat{v}_m) c_d^{\max} \|\vec{v}_d\|}{\max(0, \hat{v}_a \cdot \hat{v}_m) \|\vec{v}_a\| + \max(0, \hat{v}_d \cdot \hat{v}_m) \|\vec{v}_d\|}. \quad (12)$$

The clamping of the inner product in Eq. 12 guarantees positive contributions to concentration transport. Fig. 3 shows the different directions of unified mean and maximum velocity fluxes for $c_a \neq c_d$.

This decomposition enables us to trace integral lines of advective, diffusive, and unified fluxes in the same way.

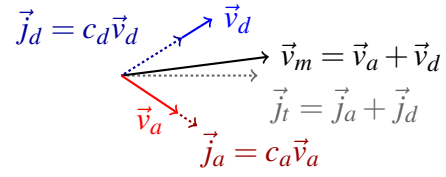


Figure 3: Construction of the direction of unified maximum velocity flux. If $c_d \neq c_a$, the directions of unified mean velocity flux $\vec{j}_a + \vec{j}_d$ and maximum velocity $\vec{v}_a + \vec{v}_d$ are different.

5. Visualization of Fluxes Using Stream Feathers

The final visualization uses the velocity and concentration values deduced from the advective, diffusive and unified fluxes. Integral lines can now be calculated which follow either of the fluxes using numerical integration. The resulting polylines are visualized using *stream tubes* which are constructed in an OpenGL geometry shader.

In case advection and diffusion carry concentrations in different directions, we extend the stream tube to a novel visualization metaphor, the *stream feathers*. Stream feathers provide a convenient way to visualize additional, diverging fluxes in a unified manner. As the unified fluxes are a combination of diffusive and advective flux, \vec{j}_t (\vec{j}_m), \vec{j}_a , and, \vec{j}_d are coplanar. If \vec{j}_d or \vec{j}_a strongly deviate from \vec{j}_t or \vec{j}_m in case

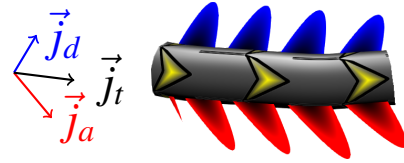


Figure 4: Stream feathers are able to capture different flux components in an intuitive combined view. The barbs of the feathers point in the direction of fluxes strongly deviating from the flux visualized as stream tube.

of the mean or maximum diffusion velocity, respectively, we draw small planar appendages like barbs of a feather to the stream tubes pointing in the direction of the deviating fluxes as shown in Fig. 4. This way, we are able to steer attention to areas of strongly divergent advective and diffusive fluxes.

In order to show the flux direction, stream tubes are textured with arrows. The size and spacing of arrows is proportional to the velocity of transport. The stream tube thickness is scaled according to the transported concentration. By mapping velocity and concentration to different visual qualities, we are not only able to show the magnitude but also the ratio of velocity and concentration of the flux. To prevent visual clutter, feather barbs are only displayed if the angle between fluxes exceeds a user-defined threshold

$\varepsilon > 1 - \|(\hat{j}_i \cdot \hat{j}_d)\|$. The length of barbs is scaled with their respective flux magnitude. Additionally, stream tubes can be colored according to the flux that most contributes to the unified flux so that the driving transport mechanism can easily be identified as shown in Fig. 1. We use a fix color pattern to highlight advective (red) and diffusive (blue) contributions.

6. Advective-Diffusive Fluxes in SPH

We apply our advective-diffusive flux visualization framework to SPH-based simulation. In Sec. 6.1 we give a very brief introduction to SPH and Sec. 6.2 discusses the extension required for flux computations in SPH.

6.1. Smoothed Particles Hydrodynamics SPH

In SPH, continuous fields are described by a finite set of particles i which carry local information about field quantities Q_i , like concentration, at particle positions \mathbf{x}_i . Reconstruction of quantities at arbitrary positions \mathbf{x} reads

$$Q(\mathbf{x}) = \sum_j Q_j V_j W_j(\mathbf{x}), \quad (13)$$

where V_i is the particle's dynamic volume and $W_j(\mathbf{x}) = W(\|\mathbf{x} - \mathbf{x}_j\|, h_j)$ is a radially symmetric smoothing kernel with finite support h_j [Mon05].

Particles change their positions according to forces acting on them. These forces include viscosity, surface tension, pressure [SP09] and external forces calculated by a discretized version of the Navier-Stokes-Equation [MCG03, Mon05]. The concentration of a particle is moved with the particle, however, particle concentrations are changed over time by diffusion and chemical reactions. The time rate of change of concentration c due to diffusion follows Fick's law as $\frac{\partial c}{\partial t} = D \nabla^2 c$ [ALS09], which for SPH particle concentrations c_i can be expressed as [Bro85]

$$\frac{dc_i}{dt} = 2D \sum_j (c_i - c_j) \frac{V_i + V_j}{2} \frac{\mathbf{x}_i - \mathbf{x}_j}{\|\mathbf{x}_i - \mathbf{x}_j\|^2} \cdot \nabla W_j(\mathbf{x}_i). \quad (14)$$

Additionally, chemical reactions and surface diffusion can be applied which result in additional concentration changes over time as described in [OHB*13].

6.2. Flux Calculation

We reconstruct advective flux from simulated data at arbitrary positions as

$$\vec{j}_a(\mathbf{x}) = \left(\sum_j c_j V_j \hat{W}_i(\mathbf{x}) \right) \left(\sum_j \vec{v}_j V_j \hat{W}_i(\mathbf{x}) \right). \quad (15)$$

We apply a *corrected SPH (CSPH)* formulation in order not to underestimate field quantities in areas of neighborhood deficiency. Here, the kernel function in Eq. (13) is corrected by replacing W_j with

$$\hat{W}_j(\mathbf{x}) = \frac{W_j(\mathbf{x})}{\sum_k V_k W_k(\mathbf{x})} \quad (16)$$

yielding zeroth order consistent interpolation [BK02].

The diffusive flux first is evaluated at particle positions as

$$\vec{j}_d(\mathbf{x}_i) = -D \sum_j (c_i - c_j) \frac{V_i + V_j}{2} \nabla W_j(\mathbf{x}_i) \quad (17)$$

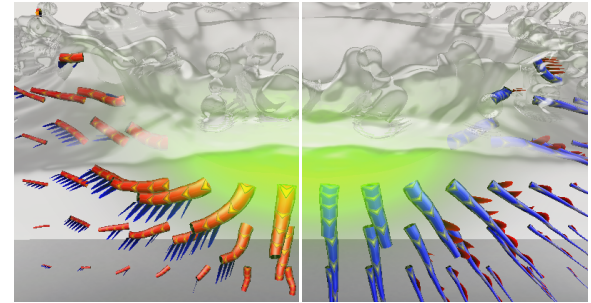
and is then approximated at arbitrary positions using corrected SPH

$$\vec{j}_d(\mathbf{x}) = \sum_j \vec{j}_d(\mathbf{x}_j) V_j \hat{W}_j(\mathbf{x}). \quad (18)$$

7. Results and Discussion

In order to demonstrate the benefits of our novel advection-diffusion visualization, we set up several example scenes.

The first scene simulates dripping a solute dye into a tank of solvent (see Figs. 1, 5, 6). At first, diffusion and advection of dye work in the same direction. After impact, advection slows down due to water pressure and the water begins to bounce back around the site of impact. Fig. 5 shows the advective and diffusive fluxes shortly after impact, corresponding to the unified mean velocity flux on the right hand side of Fig. 1. Diffusion transports concentration perfectly radially away from the site of impact. Stream feathers nicely accentuate areas of divergent advective and diffusive fluxes which would have not been revealed otherwise.



(a) Advective flux with diffusion feathers (b) Mean velocity diffusive flux with advection feathers

Figure 5: Stream feather visualization of advective and diffusive fluxes corresponding to the unified mean velocity flux in Fig. 1, right.

Fig. 6 shows the situation about 6s after impact when the water is still bouncing. The advective movement clearly slows down and diffusion dominates the total transport. At this point in time, advection and diffusion work in the same direction around the site of impact, hence, stream feathers are not visible in that region. The coloring according to the dominating flux is still able to convey the respective contributions of advection and diffusion to the total transport.

In the second scene we drip pure solvent into a tank of

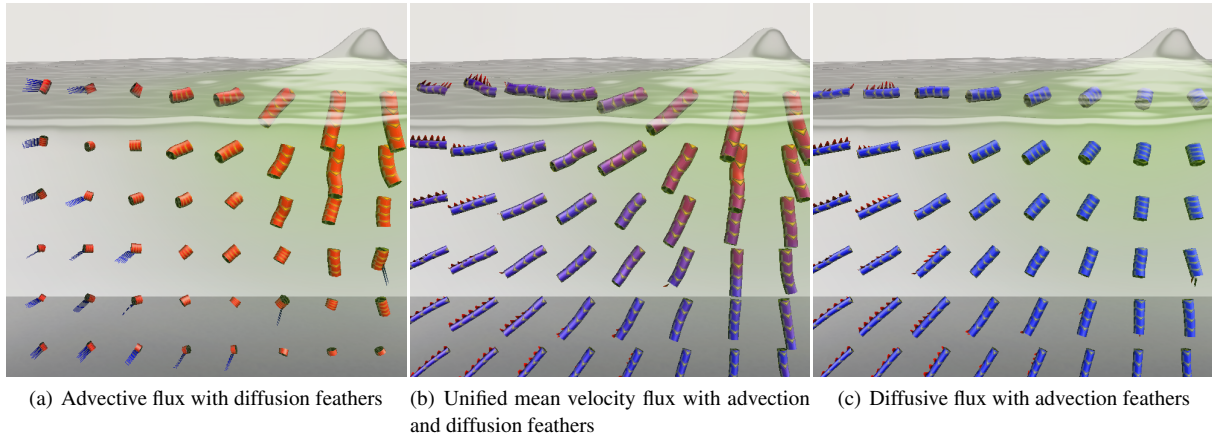


Figure 6: Advective, unified mean velocity and diffusive fluxes after impact of dye in solvent (see Fig. 1). Diffusion radially transports concentration away from the site of impact and dominates the flow farther away from the impact site. Advection due to bouncing water dominates the flow near the impact site.

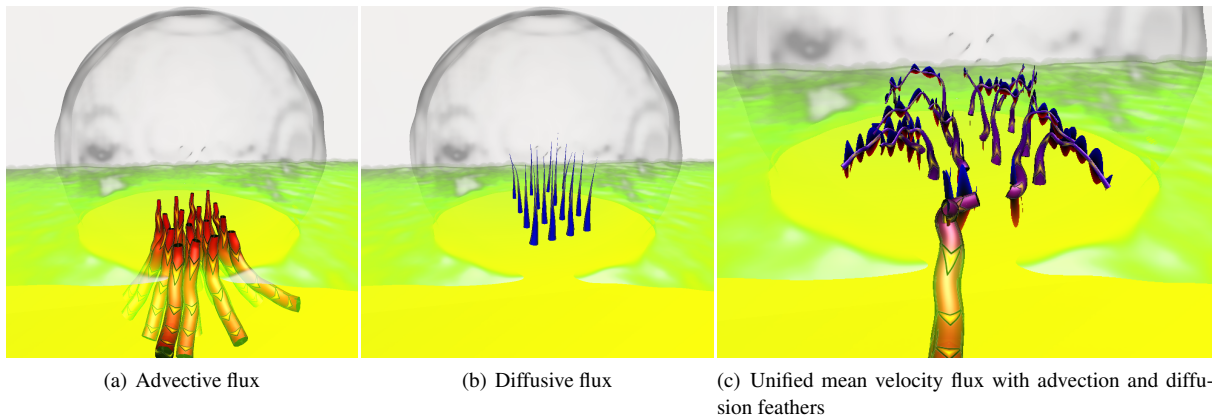


Figure 7: Advective, diffusive and unified mean velocity fluxes at impact of a solvent drop in a tank of dye. Advection and diffusion work in opposite direction.

solute dye as an example for counteracting advection and diffusion. Fig. 7 shows the situation shortly after impact of the solvent drop. At that point in time, diffusion transports dye into the drop (Fig. 7(b)) at nearly the same velocity as the drop's downward advective motion (Fig. 7(a)) so that the unified mean velocity flux nearly gets perpendicular to both the advective and diffusive fluxes as shown in Fig. 7(c). The stream feathers and the colored stream tubes are able to intuitively convey this situation of opposite fluxes.

The third scene shown in Fig. 8 demonstrates the utility of our visualization in a real-world application. We simulate the mixing of solute dye and solvent in a t-sensor [KWFY99]. In the t-sensor the dye and solvent streams on the left are accelerated by pressure. The two streams meet at the junction of the t-sensor and merge to one stream which can be analyzed.

In the lower left of the t-sensor, back-diffusion of concentration in the opposite direction of the advection of the solvent stream takes place.

A standard stream tube visualization of the velocity field (Fig. 8(a)) can not convey the magnitude of advective flux. In contrast, our visualization of advection (Fig. 8(b)) intuitively shows the magnitude of transport by scaling the tube thickness according to the transported concentration while the velocity is captured by the arrow size and spacing. The additional stream feathers show the diverging direction of diffusive flux. The visualization of maximum velocity diffusion (Fig. 8(d)) can give insight into diffusive transport in regions in which the Einstein model smoothes velocities (Fig. 8(c)) causing stream tubes to degenerate. In both visualizations of diffusion, stream feathers intuitively reveal the diverging

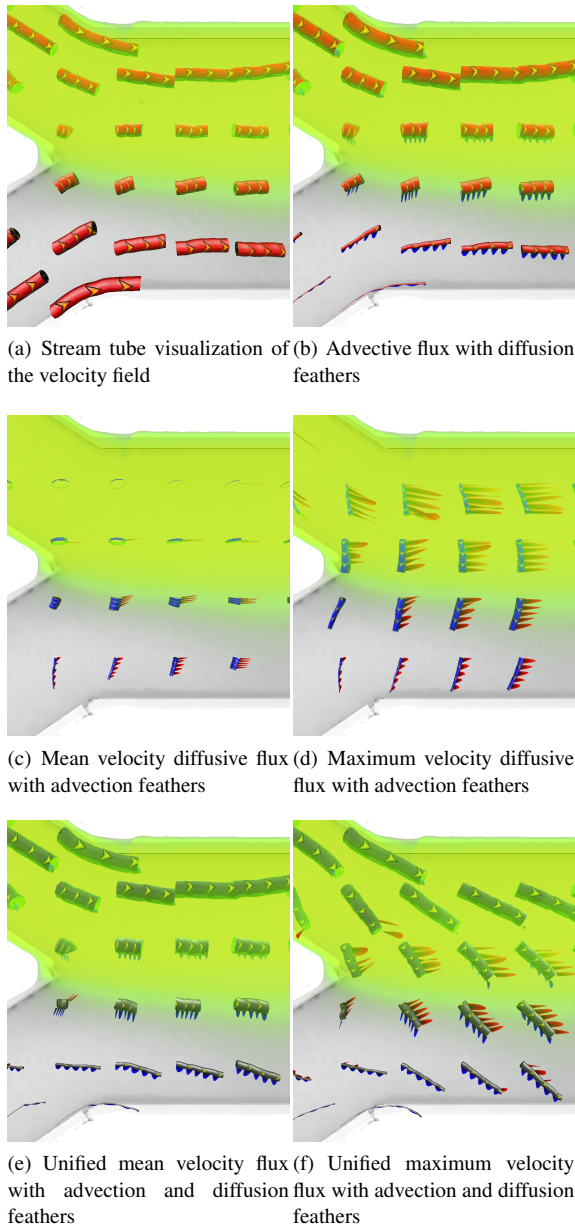


Figure 8: Advective, diffusive and unified fluxes of the flow in a *t*-sensor. Note how advective and diffusive fluxes transport concentration in nearly perpendicular directions.

direction of advection. The unified maximum velocity flux (Fig. 8(f)) more clearly reveals the back-diffusion that takes place in the lower left stream compared to the visualization of unified mean velocity flux (Fig. 8(e)). The stream feathers are scaled according to the magnitude of their respective fluxes and nicely capture the nearly perpendicular directions of advection and diffusion.

Compared to simple glyph-based renderings our stream tubes do not only encode magnitude and direction of flux but can reveal the ratio of velocity and concentration of transport by mapping these entities to stream tube thickness and arrow spacing, respectively. Important additional information is added by simultaneously showing deviating flux directions as feathers. A drawback of our approach, however, is the fact that the length of stream feathers, i.e. the flux magnitude, and the spacing between arrows, i.e. the velocity, cannot directly be compared.

The last scene is an artistic setup of a tank containing a 3D checker board pattern of different dye concentrations in solvent. From above, a quad of solute dye drops into the tank. Thus, the advection follows a classic dam break scenario. The checker board pattern of concentrations in the fluid bulk causes a distinct pattern of diffusion. Fig. 9 shows the development of the scenario over time for three different time steps. At first (Fig. 9(a)), diffusion and advection take place in separated areas: Diffusion is restricted to the fluid bulk and advection to the falling fluid quad. As soon as the fluid quad hits the tank (Fig. 9(b)), fluid in the tank gets displaced. Hence, the diffusive flux in the tank is superimposed by a strong advective flux. The regions of strongly diverging fluxes at the edges of the checker board pattern are again emphasized by the stream feather rendering. The red coloring of the stream tubes clearly indicates that advection is the driving force in the upper half of the fluid. In the lower half, however, diffusion still is dominant. The movement of the quad continues to displace fluid and effectively creates a wave that travels to the right (Fig. 9(c)). The stream feathers and the coloring still clearly indicate that diffusion plays an important role for total transport and should not be neglected in visualization.

All integral lines are directly computed from raw simulation data using a CUDA implementation. Time integration of streamlines has been realized using a fourth order Runge-Kutta scheme with fixed time step for a fixed duration of time. Streamlines have been generated from a planar grid of seed points that can be interactively controlled by the user. Calculations have been carried out on an Intel Core i7 930 at 2.8 GHz with 24 GiB RAM and on an NVIDIA GTX Titan with 6 GiB of VRAM. Table 1 gives timings of both our integral line calculations and our renderings of stream feathers. The timings denoted by ‘Drop’ in the table apply to both drop scenarios. Our timings clearly show that in all scenes we achieved interactive frame rates both for the generation of streamlines and the rendering of stream feathers allowing for a direct exploration of simulation data. As we operate directly on raw data, our visualization can already be used during simulation. The computation time for streamlines is mainly dominated by the amount of samples along a streamline and not by the number of streamlines which is due to our parallel CUDA implementation.

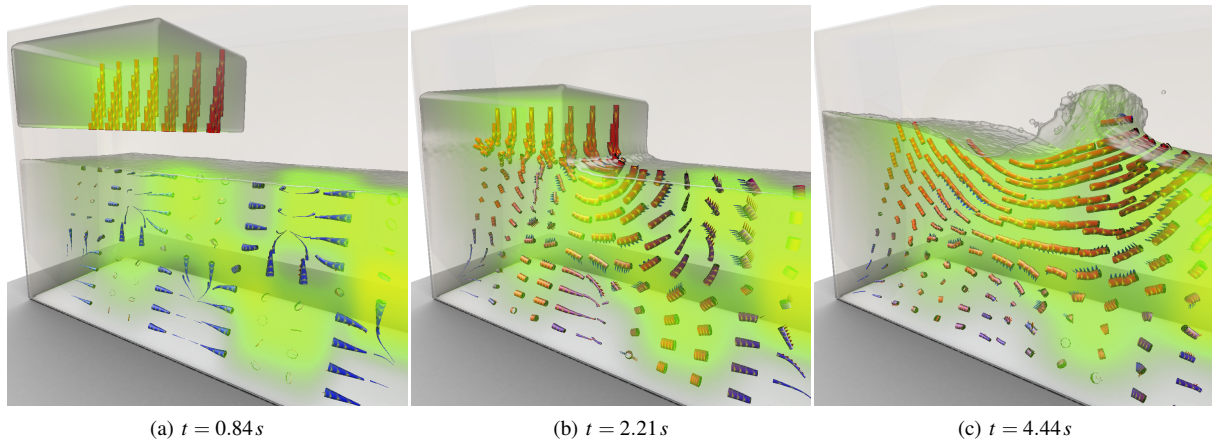


Figure 9: Unified mean velocity flux of the checker board scene over three time steps. The quad of solute dye (Fig. 9(a)) moves downward and hits the surface of the tank (Fig. 9(b)) causing a superposition of the initially separated advective and diffusive fluxes. The impact causes a wave to form (Fig. 9(c)) that travels to the right causing a strong advective flux.

Table 1: GPU timings of streamline integration and stream feather rendering for our test scenarios. The first column names the scenario and gives the number of simulated particles (in Mio.). Res. is the seeder plane resolution. The duration (integration time) of the streamline and the stepsize for the Runge-Kutta integration are given in Dur. and Step, respectively. Int. denotes the calculation time for the streamlines and Vis. is the frame rate of rendering stream feathers.

Scene (#Mio. ptcls)	Res.	Dur. (s)	Step (ms)	Int. (ms)	Vis. (fps)
T-Sensor (0.58)	64 × 64	0.75	2.5	270	32
	4 × 4	2		240	60
Drop (1.16)	64 × 64	1	5	145	32
		2		240	16
Checker Board (1.34)	32 × 32	1		171	60
		2	7.5	300	60
	64 × 64	1		171	46
		2		305	23

8. Conclusions

We presented a framework for simultaneous visualization of advective, diffusive and unified fluxes based on integral lines. The main goal is to provide insight into the intrinsic structure of the concentration transport and the relation between the diffusive and the advective components. As integral lines require a velocity field, we decompose the diffusive and the unified flux into a velocity and a concentration part based on the concept of mean and maximum diffusion velocity, yielding the unified mean and maximum velocity fluxes, respectively. Using our new metaphor of stream feathers, we can simultaneously visualize the combined advection-diffusion processes.

Our proposed decomposition of fluxes and the visualiza-

tion for advective-diffusive flows can be applied to any kind of (simulation) data which provides velocity and concentration data. We apply our approach to SPH-based flow simulations and demonstrate methods for a stable reconstruction of continuous advective and diffusive flux fields in SPH.

Benefits: Evaluating our new visualization approach shows that it nicely reveals situations with divergent advective and diffusive fluxes. Both approaches, the unified mean and maximum velocity fluxes, give clear hints to the intrinsic nature of the superimposed concentration transport mechanisms. In cases of high concentrations the Einstein model strongly decreases velocities. Here, the unified maximum velocity flux more clearly reveals effects like back-diffusion. Thus, both approaches complement each other in their expressiveness.

Limitations: By tracing either mean or maximum velocity diffusive fluxes, we don't fully reflect the random nature of diffusion, as it statistically spreads concentrations uniformly. In areas of high concentration and small diffusion gradients, stream tubes of mean diffusive flux can degenerate. In this case using the maximum velocity diffusion model can still reveal all relevant information of diffusion.

Acknowledgments

We greatly appreciate preliminary discussions with Sergey Druzhinin. We are very grateful to Martin Pätzold for discussions and for preparing the video and to Willi Gräfrath for giving the video a voice.

References

- [AIAT12] AKINCI G., IHMSEN M., AKINCI N., TESCHNER M.: Parallel surface reconstruction for particle-based fluids. *Comput. Graph. Forum* 31 (2012), 1797–1809. 3

- [ALS09] ADAM G., LÄUGER P., STARK G.: *Physikalische Chemie und Biophysik*. Springer-Lehrbuch. Springer, 2009. 6
- [BCP*12] BRAMBILLA A., CARNECKY R., PEIKERT R., VIOLA I., HAUSER H.: Illustrative Flow Visualization: State of the Art, Trends and Challenges. In *EG 2012 - State of the Art Reports* (Cagliari, Italy, 2012), Cani M.-P., Ganovelli F., (Eds.), Eurographics Assoc., pp. 75–94. 2
- [BK02] BONET J., KULASEGARAM S.: A simplified approach to enhance the performance of smooth particle hydrodynamics methods. *J. Appl. Math. & Computation* 126, 2-3 (2002), 133–155. 6
- [BPR01] BÜRKLE D., PREUSSER T., RUMPF M.: Transport and anisotropic diffusion in time-dependent flow visualization. In *Proceedings of the Conference on Visualization '01* (Washington, DC, USA, 2001), VIS '01, IEEE Computer Society, pp. 61–68. 2
- [Bro85] BROOKSHAW L.: A method of calculating radiative heat diffusion in particle simulations. In *Astronomical Society of Australia* (1985), vol. 6, pp. 207–210. 6
- [BSL07] BIRD R., STEWART W., LIGHTFOOT E.: *Transport Phenomena*. Wiley, 2007. 2, 5
- [CL93] CABRAL B., LEEDOM L. C.: Imaging vector fields using line integral convolution. In *Proc. of the 20th Annu. Conf. on Comput. Graph. Interactive Techniques* (New York, NY, USA, 1993), SIGGRAPH '93, ACM, pp. 263–270. doi:10.1145/166117.166151. 1, 2
- [Cus09] CUSSLER E.: *Diffusion: Mass Transfer in Fluid Systems*. Cambridge Series in Chemical Engineering. Cambridge University Press, 2009. 4
- [DH93] DELMARCELLE T., HESSELINK L.: Visualizing second-order tensor fields with hyperstreamlines. *IEEE Comput. Graph. Appl.* 13, 4 (July 1993), 25–33. doi:10.1109/38.219447. 2
- [DPR00] DIEWALD U., PREUSSER T., RUMPF M.: Anisotropic diffusion in vector field visualization on euclidean domains and surfaces. *IEEE Trans. Vis. Comput. Graph.* 6, 2 (Apr. 2000), 139–149. doi:10.1109/2945.856995. 2
- [EHK*06] ENGEL K., HADWIGER M., KNISS J. M., REZK-SALAMA C., WEISKOPF D.: *Real-time Volume Graphics*. A. K. Peters, Ltd., Natick, MA, USA, 2006. 1, 2
- [Ein05] EINSTEIN A.: Über die von der molekularkinetischen Theorie der Wärme geforderte Bewegung von in ruhenden Flüssigkeiten suspendierten Teilchen. *Annalen der Physik* 322, 8 (1905), 549–560. doi:10.1002/andp.19053220806. 3, 4
- [FAB*11] FELL D., AUERNHAMMER G. K., BONACCURSO E., LIU C., SOKULER R., BUTT H.-J.: Influence of surfactant concentration and background salt on forced dynamic wetting and dewetting. *Langmuir* 27, 6 (2011), 2112. 2
- [FAW10] FRAEDRICH R., AUER S., WESTERMANN R.: Efficient high-quality volume rendering of SPH data. *IEEE Trans. Vis. Comput. Graph.* 16, 6 (2010), 1533–1540. 3
- [FW12] FRAEDRICH R., WESTERMANN R.: Motion visualization of large particle simulations. In *Proceedings of IS&T/SPIE Electronic Imaging 2012, Conference on Visualization and Data Analysis* (2012), SPIE, pp. 82940Q–1 – 12. 3
- [JH04] JOHNSON C., HANSEN C.: *Visualization Handbook*. Academic Press, Inc., Orlando, FL, USA, 2004. 3
- [KSW*12] KARCH G. K., SADLO F., WEISKOPF D., MUNZ C.-D., ERTL T.: Visualization of advection-diffusion in unsteady fluid flow. *Comput. Graph. Forum* 31, 3pt2 (2012), 1105–1114. doi:10.1111/j.1467-8659.2012.03103.x. 2, 3
- [KW06] KINDLMANN G., WESTIN C.-F.: Diffusion tensor visualization with glyph packing. *IEEE Trans. Vis. Comput. Graph.* 12, 5 (Sept.–Oct. 2006), 1329–1335. 2
- [KWFY99] KAMHOLZ A. E., WEIGL B. H., FINLAYSON B. A., YAGER P.: Quantitative analysis of molecular interaction in a microfluidic channel: the t-sensor. *Analytical Chemistry* 71, 23 (1999), 5340–5347. 2, 7
- [KWH00] KINDLMANN G., WEINSTEIN D., HART D.: Strategies for direct volume rendering of diffusion tensor fields. *IEEE Trans. Vis. Comput. Graph.* 6, 2 (Apr.–June 2000), 124–138. doi:10.1109/2945.856994. 3
- [MCG03] MÜLLER M., CHARYPAR D., GROSS M.: Particle-based fluid simulation for interactive applications. In *Proc. Symp. Comp. Anim.* (2003), pp. 154–159. 6
- [MLP*10] MCLOUGHLIN T., LARAMEE R. S., PEIKERT R., POST F. H., CHEN M.: Over two decades of integration-based, geometric flow visualization. *Comput. Graph. Forum* 29, 6 (2010), 1807–1829. 1, 2
- [Mon05] MONAGHAN J. J.: Smoothed particle hydrodynamics. *Reports on Progress in Physics* 68 (2005), 1703–1759. 6
- [MS93] MA K.-L., SMITH P.: Cloud tracing in convection-diffusion systems. In *Proc. IEEE Vis.* (Oct 1993), pp. 253–260. doi:10.1109/VISUAL.1993.398876. 2
- [OHB*13] ORTHMANN J., HOCHSTETTER H., BADER J., BAYRAKTAR S., KOLB A.: Consistent surface model for SPH-based fluid transport. In *Proc. Symp. Comp. Anim.* (2013), pp. 95–103. 6
- [OKK10] ORTHMANN J., KELLER M., KOLB A.: Topology-caching for dynamic particle volume raycasting. In *Proc. Vision, Modeling & Visualization (VMV)* (2010), pp. 147–154. 3
- [Sch96] SCHNOOR J.: *Environmental modeling: fate and transport of pollutants in water, air, and soil*. Environmental science and technology. J. Wiley, 1996. 3
- [SFBP09] SCHINDLER B., FUCHS R., BIDDISCOMBE J., PEIKERT R.: Predictor-corrector schemes for visualization of smoothed particle hydrodynamics data. *IEEE Trans. Vis. Comput. Graph.* 15, 6 (2009), 1243–1250. 3
- [SKE14] SADLO F., KARCH G. K., ERTL T.: Topological features in time-dependent advection-diffusion flow. In *Topological Methods in Data Analysis and Visualization III* (2014), Bremer P.-T., Hotz I., Pascucci V., Peikert R., (Eds.), Springer, pp. 217–231. 2, 3
- [SP09] SOLENTHALER B., PAJAROLA R.: Predictive-corrective incompressible SPH. *ACM Trans. Graph.* 28 (2009), 40:1–40:6. 6
- [WKL99] WEINSTEIN D., KINDLMANN G., LUNDBERG E.: Tensorlines: Advection-diffusion based propagation through diffusion tensor fields. In *Proc. IEEE Vis.* (1999), pp. 249–253. 2